

# Propagation-based phase-contrast X-ray microtomography of a cerebral protection device retrieved after carotid artery stenting

Sung Won Youn,<sup>a\*</sup> Ho Kyun Kim,<sup>a</sup> Hong Tae Kim,<sup>b\*</sup> Sung Mi Han,<sup>b</sup> Jin Kuk Do,<sup>c</sup> Young Rok Do,<sup>c</sup> Hui Joong Lee,<sup>d</sup> Jongmin Lee<sup>d</sup> and Jae Hong Lim<sup>e</sup>

<sup>a</sup>Department of Radiology, Catholic University of Daegu School of Medicine, Daegu, Republic of Korea, <sup>b</sup>Department of Anatomy, Catholic University of Daegu School of Medicine, Daegu, Republic of Korea, <sup>c</sup>Department of Neurology, Catholic University of Daegu School of Medicine, Daegu, Republic of Korea, <sup>d</sup>Department of Radiology, Kyungpook National University School of Medicine, Daegu, Republic of Korea, and <sup>e</sup>X-ray Imaging Group, Beamline Division, Pohang Accelerator Laboratory, POSTECH, Pohang, Gyungbuk, Republic of Korea.

\*E-mail: ysw10adest@cu.ac.kr, htaekim@cu.ac.kr

Phase-contrast synchrotron X-ray microtomography (pcSyncX) based on the highly coherent X-ray beam has previously been used to visualize the microstructures of biologic specimens, but it has never been used to evaluate embolic debris adherent on a cerebral protection device (CPD). The purpose of this study was to demonstrate the feasibility of pcSyncX for evaluating embolic debris during carotid artery stenting (CAS). Five patients (four males, age range 67–77 years) with severe carotid artery stenosis underwent CAS. The retrieved CPD was exposed to synchrotron radiation and 1000 pcSyncX projection images were obtained by rotating the CPD through 180°. An X-ray shadow of a CPD was converted into a visual image by the scintillator. After microtomographic reconstruction, the three-dimensionally reconstructed images were further segmented into the embolic debris and CPD. The total volume of emboli was calculated by summing the volume at each scanning level. The number of membrane pores covered by emboli as seen from the outer surface was counted and the percentage of covered area was calculated. Embolic debris was clearly demonstrated not only on the inner surface and within pores but also on the outer surface of the CPD. The mean total volume of embolic debris was  $0.538 \times 10^{-6} \text{ mm}^3$  (range  $0.225\text{--}0.965 \times 10^{-6} \text{ mm}^3$ ). Most (61.5%) of the debris was located at the apical one-third of the CPD and 20.8% of the pore area was covered by debris.

**Keywords:** phase contrast; synchrotron X-rays; microtomography; embolic debris; cerebral protection device; carotid artery stenting.

© 2014 International Union of Crystallography

## 1. Introduction

Carotid artery stenting (CAS) has emerged as an effective treatment for carotid artery stenosis and is being increasingly performed due to the advent of cerebral protection devices (CPDs) to filter embolic debris (CAVATAS Investigators, 2001; Castriota *et al.*, 2002; Wholey *et al.*, 2003). Various types of CPDs have been used to reduce the risk of embolic events and thereby increase the safety of CAS (Cremonesi *et al.*, 2003; Kastrup *et al.*, 2003; EVA-3S Investigators, 2004; Yadav *et al.*, 2004). Nevertheless, caution is required when using a CPD in order to prevent CPD-related adverse events. The CPD itself may cause transient spasm or intimal denudation, and accumulated embolic debris may be dislodged during the deployment or retrieval of CPDs (Müller-Hülsbeck *et al.*,

2005). The blood flow velocity may be decreased after the deployment of a CPD and increased after its retrieval, even in patients with normal angiographic flow (Casserly *et al.*, 2005; Roffi *et al.*, 2008; Sorimachi *et al.*, 2011). The flow impairment might be due to obstruction of the CPD pores, so reducing the total amount of embolic debris, such as by the aspiration of blood samples, may be a useful management intervention (Sorimachi *et al.*, 2010).

Until recently, the evaluation of the burden of embolic debris has been dependent upon visual inspection or performed using optical microscopy (Angelini *et al.*, 2002; Rogers *et al.*, 2004; Quan *et al.*, 2005; Hayashi *et al.*, 2009) or electron microscopy (DeRubertis *et al.*, 2007; Brightwell *et al.*, 2011). However, optical and electron microscopy require multiple steps of staining and thin-slice dissection. Moreover,

**Table 1**

Lesion characteristics and procedural events.

ID, identification number of patient. Age is in years. M, male; F, female. % Stenosis, stenosis rate determined by criteria of the North American Symptomatic Carotid Endarterectomy Trial. #BAL, number of balloon dilatations at pre-stenting/post-stenting steps. TE, thromboembolic event. FA, flow arrest related to the cerebral protection device (CPD). BDZ, infarct in border zone. F, frontal cortex. FP, frontoparietal cortex. N, none. SZ, seizure. BAL, balloon dilatation. HR, heart rate. BP, blood pressure.

ID	Age/Sex	Brain lesion	% Stenosis, before/after	#BAL	TE/FA	Other events
1	72/M	BDZ, several tiny acute	Right, 60.0/0	1/0	N/N	Transient SZ during BAL
2	67/M	F, a few tiny acute	Left, 69.8/0; right, 55.4/0	2/0, 2/0	N/N	Low HR, improved
3	77/F	FP, several small acute	Left, 88.0/0	3/0	N/N	Low HR and BP, improved
4	75/M	Corona radiata, small acute BDZ, old	Left, 61.2/2.7	2/0	N/N	Low HR, improved
5	77/M	None (amaurosis fugax)	Right, 83.2/10.4	1/1	N/N	None

after dissection it might not be easy to recognize how the microscopic features of a specimen are correlated with its gross appearance, thereby making it difficult to quantify the total volume of the debris or the debris volumes at different locations.

Synchrotron radiography, which can avoid the need for dissection, has been used to depict detailed microstructures of various biomaterials both under *in vivo* and *ex vivo* conditions (Takeda *et al.*, 2000; Koh *et al.*, 2006; Shinohara *et al.*, 2008; Choi *et al.*, 2010; Coan *et al.*, 2010), but it has not been used previously for evaluating the embolic debris adherent on a CPD. In synchrotron radiography, the edges between different regions of an object with different refractive indices induce slight deviations in the well collimated X-ray beam, and the resulting edge enhancement produces high-spatial-resolution images that are based on phase shifts rather than X-ray absorption (Meuli *et al.*, 2004).

The purpose of this study was to demonstrate the feasibility of phase-contrast synchrotron X-ray microtomography (pcSyncX) as a tool for evaluating the embolic debris adherent on a CPD during CAS.

**2. Materials and methods**

**2.1. Study design and inclusion criteria**

This prospective study enrolled five patients (four males, median age 75 years, age range 67–77 years) who underwent CAS with a CPD between June and December 2010 (Table 1). The study complied with the Declaration of Helsinki and was approved by our institutional review board. Written informed consent for the procedure was obtained from all patients. All patients had symptomatic stenosis, and acute brain lesions were seen at the cortex (*n* = 2), border zone (*n* = 1) and corona radiata (*n* = 1) on an MRI scan prior to stenting. Patient 5 presented with amaurosis fugax without an acute infarct. Catheter angiographic measurements indicated that the mean baseline stenosis [quantified as (diameter of the narrowest portion)/(diameter of the intact distal cervical carotid artery) × 100%] was 67.3%.

**2.2. Carotid artery stenting procedure**

Patients were taking aspirin (125 mg per day) and clopidogrel (75 mg per day) at least for three days before the procedure. A 3000 U bolus of heparin was administered

intravenously immediately after obtaining femoral access, with 1000 U added per hour during the procedure without checking the activated clotting time. This protocol resulted in a mean total of 4600 U of heparin being administered during the procedure. Electrocardiography (ECG) and the continuous arterial blood pressure (BP) were monitored. A 7F 90 cm-long sheath catheter (Shuttle SL Flexor, Cook, Bloomington, IN, USA) was positioned into the common carotid artery and digital subtraction angiography was performed with the use of the angiographic equipment (Integris 3000, Philips, The Netherlands). Predilatation was performed in one patient (No. 5) with a 2 mm balloon catheter (Gateway, Boston Scientific, Natick, MA, USA) before placing the CPD. After crossing the stenosis, we deployed a basket-type CPD (FilterWire EZ, Boston Scientific) whose polyurethane membrane with 110 μm pores was attached to a self-expanding nitinol ring on a guide wire (Fig. 1). Pre-stenting balloon dilatation was performed using balloon catheters with diameters of 4–6 mm (one of 4 mm, three of 5 mm and two of 6 mm), and atropine was administered when required to treat bradycardia during balloon dilatation. Self-expandable nitinol

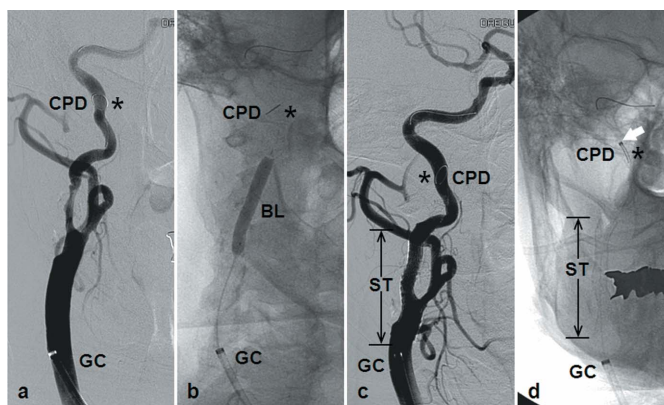


**Figure 1** The procedural steps of carotid artery stenting in patient 1. (a) A 7F guiding catheter (GC) was positioned into the right common carotid artery and a basket-type cerebral protection device (CPD) was deployed at the distal cervical segment. Its membranous portion with 110 μm pores was attached to a self-expanding nitinol ring (asterisk) on a guide wire. (b) Balloon dilatation was performed using a 5 mm × 30 mm balloon catheter (BL). (c) A 10 mm × 40 mm self-expandable nitinol stent (ST) was placed. (d) The nitinol ring (asterisk) of the CPD was collapsed by advancing the retrieval catheter (white arrow) and the CPD was removed from the GC.

stents (Precise, Cordis, Miami Lakes, FL, USA; one, three and two with diameters of 8, 9 and 10 mm, respectively) were delivered over the 0.014 inch guide wire of the CPD and placed at the stenosis. Post-stenting balloon dilatation was performed with a 6 mm balloon catheter only in patient 5. The CPD was removed from the sheath catheter at the end of CAS. The distal segment of the CPD that contained debris was cut and fixed in 10% neutral-buffered formalin. The patients were transferred to the intensive care unit with continuous ECG monitoring for 24 h following the procedure and non-invasive BP measurements were made every 2 h for at least 24 h. The patients continued taking clopidogrel for at least 30 days and the aspirin indefinitely.

### 2.3. Imaging protocol of phase-contrast synchrotron radiography

Phase-contrast synchrotron radiography was performed using the coherent synchrotron X-rays at the 7B2 beamline of the Pohang Light Source in Korea (Fig. 2). The hard X-rays used in this study were polychromatic with an energy range of 10–40 keV, because the experiments were performed before a

new imaging station equipped with a monochromator was commissioned. The X-rays emanated from a bending magnet of the electron storage ring with an electron energy of 2.5 GeV, and a typical beam current of 200 mA passed through two beryllium windows and then reached the experimental hutch located 28 m from the X-ray source. A set of high-speed X-ray shutters and polished silicon wafers (with a total thickness of 1 mm) were used to control the dose on samples. The calculated X-ray flux density was  $\sim 7 \times 10^{11}$  photons  $\text{mm}^{-2} \text{s}^{-1}$  which corresponds to  $\sim 120 \text{ Gy s}^{-1}$  for liquid water. However, the CPD samples are tiny and made of light membrane that highly transmits X-rays and indeed we observed no noticeable change of the samples before and after the microtomographic scan, which is also evidenced by the successful reconstruction of the microtomographic images. The experimental geometry and in particular the detector position were selected so as to optimize the performance of the set-up in propagation-based phase-contrast imaging. The CPD was placed 230 mm upstream of the detector in order to optimize the detection of phase-contrast effects. The CPD was fixed on a computer-controlled precision stage for performing microtomography, and an image was obtained by rotating the object with an exposure time of 100 ms for each projection. The detector system consisted of a 100  $\mu\text{m}$ -thick  $\text{CdWO}_4$  cleaved single-crystal scintillator and an optical microscope with a charge-coupled device (CCD) camera attached. The image produced by the scintillator was reflected by a mirror and then magnified by an interchangeable optical lens system with a variable magnification (the lowest is  $\times 5$ ). The magnified image was then detected by a CCD camera. One thousand projection images were obtained at different angles in  $0.18^\circ$  increments over the  $180^\circ$  of rotation. The fields of view of these images were determined by the size of the CCD chip and the optical magnification: with a  $\times 5$  microscope objective, the field of view was  $7.0 \text{ mm} \times 4.6 \text{ mm}$  because the CCD camera had an active area of  $36 \text{ mm} \times 24 \text{ mm}$  with  $4008 \times 2672$  pixels (width  $\times$  height); therefore, each pixel corresponded to approximately  $1.74 \mu\text{m} \times 1.74 \mu\text{m}$ . The spatial resolution was determined using the Xradia resolution and calibration standard pattern. The  $3 \mu\text{m}$  half-period features were distinguishable for the sample-to-detector distance of 230 mm and thus the actual resolution was  $6 \mu\text{m}$ . Three-dimensional volume images of the specimen were obtained by applying a filtered back-projection algorithm to the projection images using the *Octopus* software package (UGCT, Ghent, Belgium). Surface reconstruction and volume segmentation and rendering were performed using *Amira* software (Visualization Sciences Group, Burlington, MA, USA).

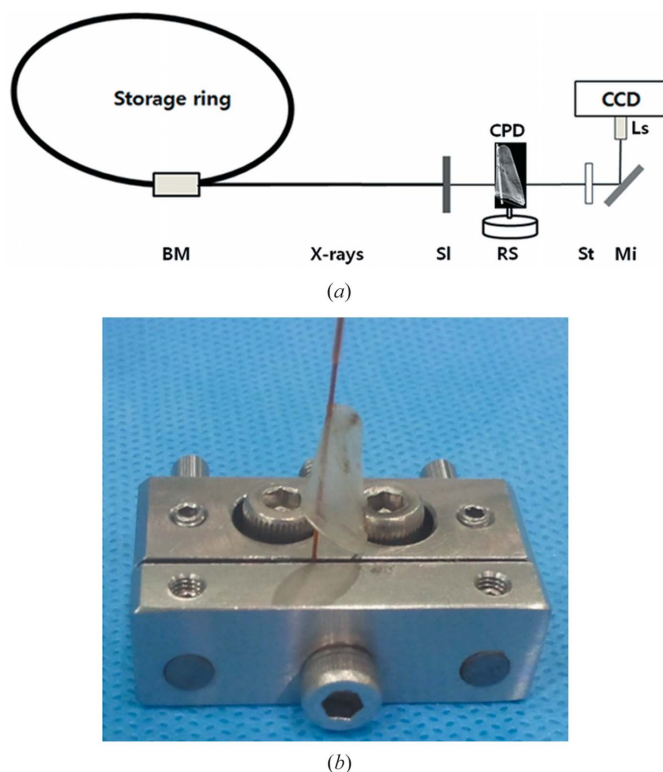


**Figure 2** Scheme of the experimental set-up of the 7B2 beamline at the Pohang Light Source. (a) The size of the polychromatic beam emanating from the bending-magnet device (BM) was reduced to match the scintillator after passing through the slit (SI). The X-rays irradiated the CPD on the rotation stage (RS) that was positioned 28 m from the X-ray source. The visual images on the surface of the  $\text{CdWO}_4$  scintillator (St) that was placed 23 cm from the object were reflected  $90^\circ$  by a gold-coated mirror (Mi) and magnified by a microscopic objective lens ( $\times 5$ ; Ls). Finally, the images reached the charge-coupled device (CCD) camera. (b) The CPD was held vertically and 1000 projection images were obtained during its rotation through  $180^\circ$ .

### 2.4. Image analysis

**2.4.1. Visual analysis.** The presence of embolic debris was evaluated in the images produced by projection and three-dimensional reconstruction (Fig. 3). By reviewing three-dimensionally reconstructed and/or cross-sectional multi-planar images (Fig. 4), the CPD was segmented into embolic debris, membrane and metallic wire. Considering the regular

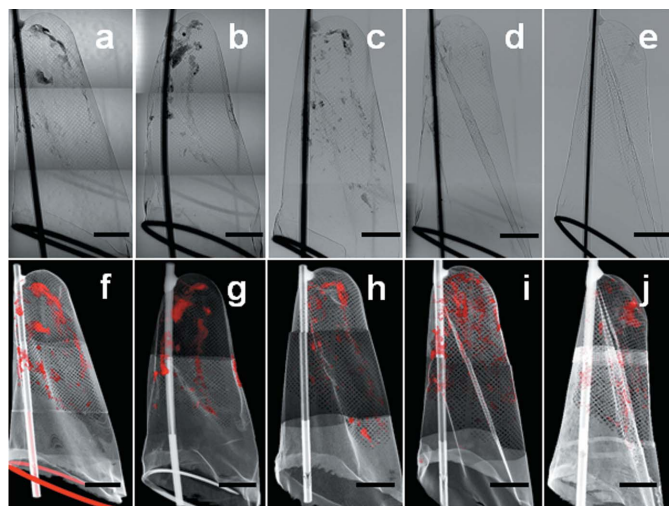


**Figure 3**  
 Visual analysis of embolic debris (ED) filtered on the CPD. (a)–(e) Projection images of patients 1–5, respectively. (f)–(j) Three-dimensionally reconstructed images of patients 1–5, respectively. The variable-size ED particles (red) after segmentation from the membrane (white) were clearly visualized in all of the patients' devices. Scale bars = 2 mm.

pattern of the porous membrane of the CPD, structures with irregular morphologic patterns (e.g. an obscured pore contour) were designated as embolic debris. The metallic wire was segmented based on its dense metallic opacity. The location of embolic debris was categorized on the inner surface, within a pore and on the outer surface of the CPD based on observations of cross-sectional views.

**2.4.2. Quantitative analysis.** The volume of the debris was determined at each longitudinal scanning level from the apex to the base of the CPD and the total volume of embolic debris was calculated by summing all of these volumes. In detail, the number of voxels constituting the embolic debris was counted with the aid of *Amira* software and then multiplied by the unit voxel volume to obtain the total volume of embolic debris (i.e. total number of voxels  $\times$  volume of each voxel). The volume of each unit voxel in the three-dimensional volume analysis was  $1.74 \text{ mm} \times 2 \text{ mm} \times 10^{-3} \text{ mm}$ , which was calculated from the cube of the two binned pixel size. The longitudinal axis of the CPD was divided into apical, middle and basal segments, and the volume of embolic debris was calculated in each segment. We also calculated the percentage area of coverage semiquantitatively by counting the pores with emboli either squeezed out or lodged within the pore. Each pore was classified into the following three patterns based on observations from the outer surface: (i) uncovered clean pores, (ii) pores plugged with tiny emboli without coalescence and (iii) pores obliterated by emboli that had been squeezed out and had coalesced on the outer surface. The number of pores with each pattern was counted, and the percentage of pores covered by embolic debris was calculated semiquantitatively as  $[\text{number of pattern (ii)} + \text{number of pattern (iii)}] / (\text{number of total pores}) \times 100\%$ . The percentage of pores that had been squeezed out onto the outer surface was calculated as  $[\text{number of pattern (iii)} / \text{number of total pores}] \times 100\%$ . The density

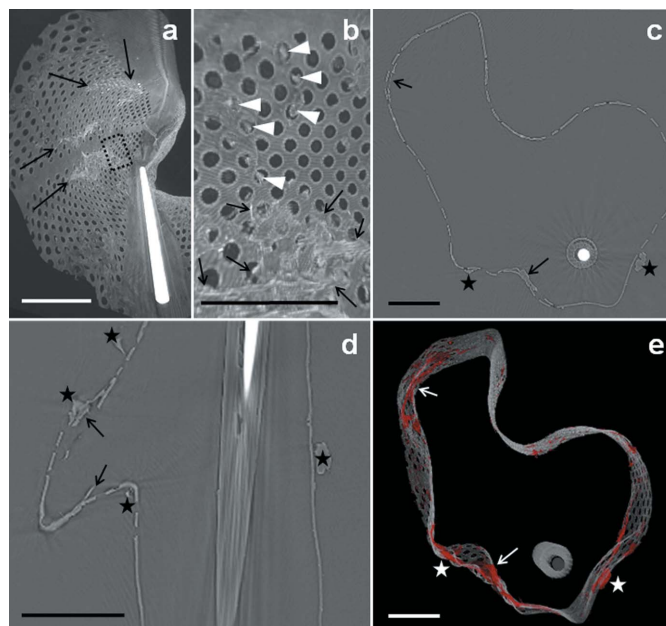


**Figure 4**  
 Localization of segmented ED from the CPD in patient 4. (a) Inner surface of the apical segment of the CPD and adherent ED (arrows) seen from the base. (b) Magnified view of the area within the rectangle in (a). Tiny debris particles were located within pores (arrowheads) and fused debris particles were attached to the inner surface of the membrane (arrows). Along with visual analysis to differentiate the ED and CPD, the segmentation procedure was performed by manually selecting contiguous debris. (c) Axial cross-sectional image. (d) Sagittal cross-sectional image. (e) Cross-sectional view of the three-dimensional reconstructed image with segmentation. ED (red) is evident in (c), (d) and (e) at the inner (arrows) and outer (asterisks) surfaces of the CPD. Scale bars = 1 mm.

values were calculated for the background, membranous CPD and embolic debris by drawing regions of interest on the source image using *Image J* (NIH, Bethesda, MD, USA). Assuming that the density of the membranous CPD is constant, the density profiles of embolic debris were shown as ratios or differences relative to the membranous CPD; the values were calculated using Excel (Microsoft, Redmond, WA, USA).

### 3. Results

#### 3.1. Procedural outcomes

The mean percentage stenosis after CAS was 2.2%. There were no cases with complications such as vasospasm, flow impairment or embolic events. However, there was one case of transient loss of consciousness during balloon dilatation and three cases of vasovagal reflex that resolved completely after the procedure. The first patient recovered consciousness with intact neurology immediately after the balloon was deflated, while the other three patients were administered fluids and dopamine until recovery. Balloon dilatation was performed a mean of two times, including one post-stenting dilatation in patient 5. The neurological examinations performed during and after the procedure did not reveal any neurological deficits.

**Table 2**

Volume, coverage area percentage and density of embolic debris (ED) measured by phase-contrast synchrotron X-ray microtomography.

Volume = number of voxels  $\times (1.74 \times 2 \times 10^{-3} \text{ mm})^3$ . Apex/total, percentage of ED captured at the apical one-third segment among its total volume. Total, total coverage area percentage is the portion of all pores that were plugged. CO, percentage of all pores that were completely obstructed by coalesced ED as seen from the outside. Mean density ratio, density of ED divided by density of the CPD ( $\times 100\%$ ), mean  $\pm$  standard deviation. Higher density proportion, proportion of ED with density more than that of the CPD relative to the background.

ID	Volume		Coverage area percentage		Density	
	Total ( $\times 10^{-6} \text{ mm}^3$ )	Apex/total (%)	Total (%)	CO (%)	Mean density ratio (%)	Higher density proportion (%)
1	0.637	68.4	17.5	6.2	86.52 $\pm$ 6.30	15.23
2	0.965	59.0	18.7	1.2	98.73 $\pm$ 6.41	55.90
3	0.359	60.0	18.8	6.4	95.97 $\pm$ 9.43	19.50
4	0.505	58.0	32.4	5.8	97.42 $\pm$ 6.98	46.52
5	0.225	62.0	17.2	3.5	97.25 $\pm$ 8.66	20.02
Average	0.538	61.5	20.8	4.6	95.18 $\pm$ 7.56	31.43

**3.2. Analysis of cerebral protection devices**

The embolic debris was successfully segmented from the CPD in all cases (Fig. 5). The various locations where debris was found are shown in Fig. 6. The larger particles of coalesced debris adhered to the membrane anchored to pores, while smaller debris particles plugged the pores (Fig. 7).

The mean total debris volume was  $0.539 \times 10^{-6} \text{ mm}^3$  (range 0.225–0.965  $\times 10^{-6} \text{ mm}^3$ ; Table 2). On average, 61.5% of the debris (range 58.0–68.4%) was located at the apical one-third segment of the CPD (Fig. 8), and 20.8% of the pore area (range 17.2–32.4%) was covered by debris. Some (mean 4.6%, range 1.2–6.4%) of the pores were completely obliterated by the embolic debris that had been squeezed out and had coalesced into contiguous pores on the outer surface of the CPD. The debris density was  $95.18 \pm 7.56\%$  (mean  $\pm$  standard

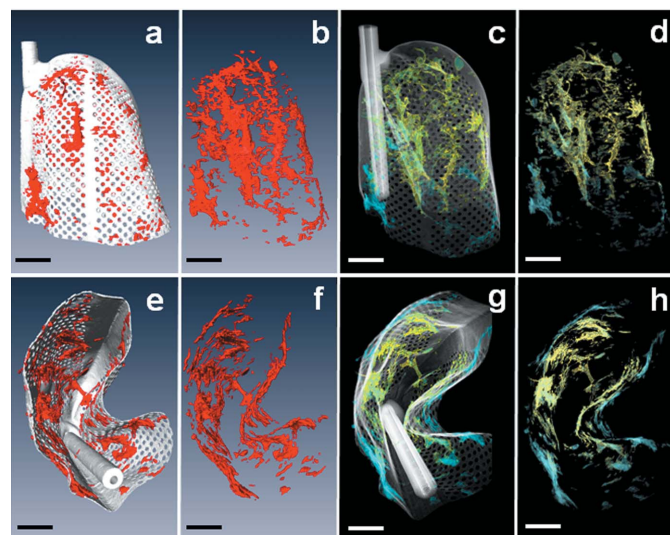


**Figure 5** Apical segment of the CPD (white) and the ED (red) in patient 4. Images in the upper row are side views, while those in the lower row are views from the base. The ED was displayed simultaneously with the CPD (a, c, e, g) and alone (b, d, f, h). (c, d, g, h) The density profiles of ED are shown in yellow, white and blue according to density ratios between ED and CPD of  $>1$ , 1 and 1, respectively. Scale bars = 1 mm.

deviation) relative to that of the membranous CPD. The density of 31.43% of the debris was higher than that of the membranous CPD.

**4. Discussion**

The presence of a smaller total burden and covered area was strongly correlated with the absence of focal neurologic deficits and CPD-related flow arrest in our patients. The total debris burden was less than  $1 \text{ mm}^3$ , which is markedly smaller than previous reports of burdens of 3–16  $\text{mm}^3$  (Rogers *et al.*, 2004; Quan *et al.*,

2005; Hill *et al.*, 2006). This discrepancy could be due to either the relatively favorable condition of our patients or the application of a more gentle procedure. Most of the debris was found at the apical segment of the CPD; such an apical predominance suggests that debris flows in a lamina pattern until it is filtered by pores of the CPD (Sorimachi *et al.*, 2010).

The size of the debris particles varied from smaller than the pore size to large enough to involve multiple pores with coalescence; however, the size distribution was not analyzed quantitatively. Some studies found most of the debris to be smaller than  $100 \mu\text{m}$  (Angelini *et al.*, 2002; Rogers *et al.*, 2004; Quan *et al.*, 2005; Hill *et al.*, 2006). Our results are consistent with these previous reports, in that 20.8% of the pores were covered and only 4.6% had materials coalescing with contiguous pores on the outer surface of the CPD. This suggests that the majority of the captured debris particles were small enough to plug a single pore. Considering that the pore size is  $110 \mu\text{m}$  and the diameter of the microcirculation is less than

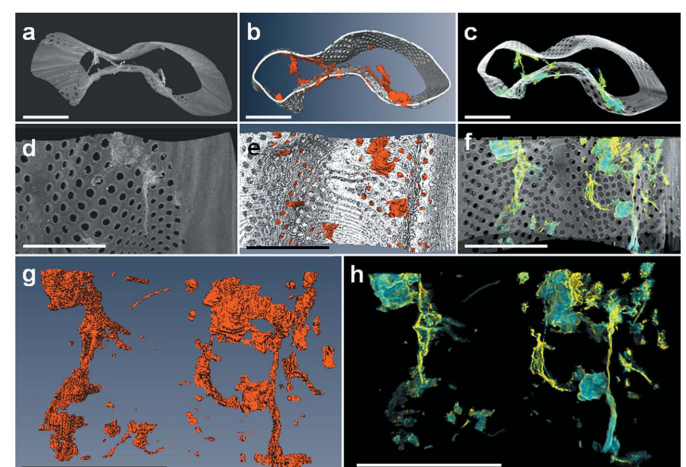


**Figure 6** Middle segment of the CPD in patient 3. ED as viewed from the base (a, b, c) and side (d, e, f). The ED particles were located on the inner surface, within a pore, and on the outer surface. (g, h) ED displayed without the CPD, allowing the total ED burden to be measured. (c, f, h) Density profiles of ED displayed as in Fig. 5. Scale bars = 1 mm.

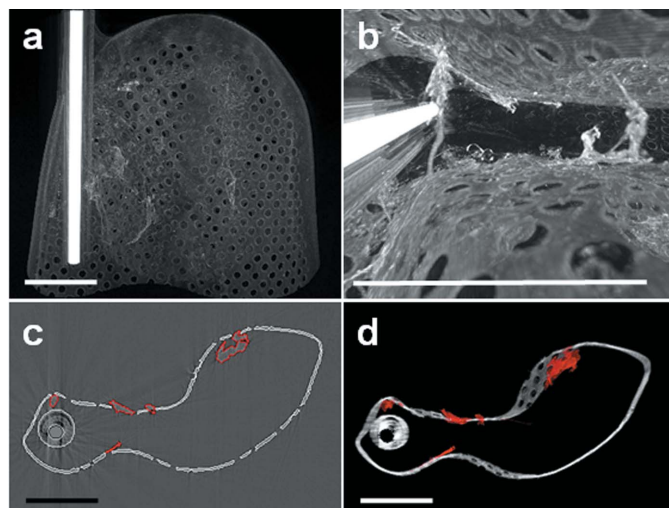


**Figure 7**  
Anchorage of ED on pores in patient 3. (a) Side view. (b) View from the base. (c) Axial cross-sectional image. (d) Cross-sectional view of three-dimensionally reconstructed image. The larger particles of coalesced debris anchored to pores, while smaller debris particles plugged the pores. Scale bars = 1 mm.

300  $\mu\text{m}$ , most debris is small enough to pass through a pore without provoking an embolic event. Therefore, the absence of focal neurologic deficits in our patients is attributable to the CPD preventing embolic events by filtering small numbers of significantly large particles of embolic debris. Moreover, no instance of filter-related flow arrest occurred, probably because the percentage of obstructed pores was much lower than the reported values that cause slow-flow (50%) and no-flow (88.5%) phenomena (Casserly *et al.*, 2005; Roffi *et al.*, 2008; Sorimachi *et al.*, 2010, 2011).

Interestingly, we found debris larger than the size of pores even on the outer surface of the CPD. We could not distinguish whether the emboli had squeezed out through the pores or had been produced locally by the aggregation of fibrin and platelets on the outer surface. Some authors have reported that retrieved thrombotic material can be produced locally inside the CPD, with various amounts of fibrin and platelet aggregates also found outside of the CPD (Piñero *et al.*, 2009). The rupturing or squeezing of atheroemboli during CAS can potentially trigger platelet aggregation and the vasoactive substances contained within a plaque or thrombus could cause vasospasm. This could in turn result in pores containing a mixture of plaque particles, fibrin and platelet aggregation reducing the blood flow through a CPD even in the presence of only small particles (Casserly *et al.*, 2005; Piñero *et al.*, 2009; Sorimachi *et al.*, 2011).

Our characterization of the debris contents involved determining the density profiles of embolic debris relative to that of the membranous CPD. However, whether the debris was composed of platelet, fibrin or plaque could not be discriminated because there are no available reference values for either their absorption densities or refractive indexes or correlations with histopathologic data. Future studies should attempt to characterize the composition of this debris, in terms

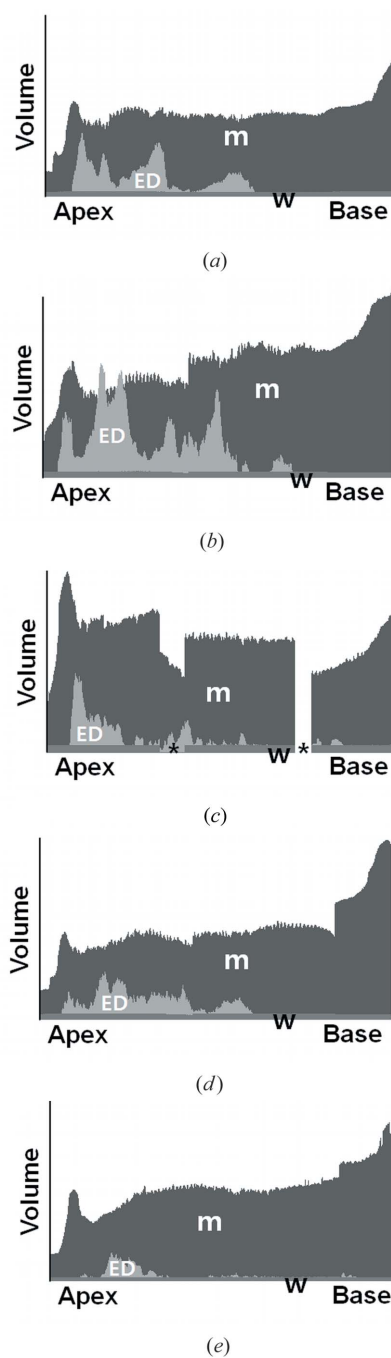


**Figure 8**  
(a)–(e) Distribution of ED along the longitudinal axis of the CPD in patients 1–5, respectively. The *x* axis represents the distance from the apex of the device, and the *y* axis represents the volume of ED. *m* is membrane, *w* is wire. The two focal interruptions in (c) (asterisks) could be artifacts from a highly radiopaque metallic wire.

of determining whether it is thrombotic, calcified, organized, fibrous or lipid-rich.

It is known that emboli are most commonly released during the CAS procedure in the step of balloon dilatation, especially after stent placement (Casserly *et al.*, 2005). We therefore used a balloon catheter with a relatively large caliber before stent placement and applied balloon dilatation only sparingly thereafter. Atherosclerotic plaques are squeezed and ruptured

during balloon dilatation, and the number of balloon dilations is significantly correlated with the presence of particles (DeRubertis *et al.*, 2007; Roffi *et al.*, 2008). Therefore, it is essential to minimize physical manipulations, including balloon dilatation, during CAS. Emboli can also be released when any device is passed through the stenosis, with the probability of such release increasing with the number of devices used. In this context, the placement of a self-expandable stent without CPD placement and balloon dilatation might have the advantage of minimizing the risk of embolization (Lownie *et al.*, 2005; Maynar *et al.*, 2007; Baldi *et al.*, 2011). However, the microscale observations from pcSyncX suggest that CPD plays its own role in filtering out even a small percentage of significantly large embolic debris particles that would potentially cause an embolic infarct if they were not filtered.

In this study we used highly coherent X-rays from synchrotron radiation, whose contrast mechanism differs from the absorption contrast involved in current clinical methods of X-ray imaging. Phase contrast is more sensitive than absorption contrast in detecting light elements and it can readily reveal weakly absorbing materials such as biological specimens. The edges between different regions of an object with different refractive indices deviate slightly for a well collimated X-ray beam. Although several phase-contrast techniques are based on the use of the refractive index as the contrast mechanism, the beauty of the experimental set-up of propagation-based phase contrast is its simplicity and its capability of real-time imaging as well as microtomography with an excellent lateral resolution of 2–5  $\mu\text{m}$  (Koh *et al.*, 2006). Considering that a CPD containing pores has many interfaces with air, the large difference of the refractive indexes of air and the CPD might contribute to edge enhancement, in addition to the large difference in the X-ray absorptions of air and CPD.

pcSyncX clearly visualized the embolic debris adherent on CPDs in all five patients of the present study, thereby demonstrating the feasibility of this modality in evaluating the function of the CPD and the safety of CAS with CPDs. The efficacy of pcSyncX was comparable with those of optical microscopy and electron microscopy, in that debris was observed in all patients (Angelini *et al.*, 2002; Rogers *et al.*, 2004; Quan *et al.*, 2005; DeRubertis *et al.*, 2007; Brightwell *et al.*, 2011). Furthermore, pcSyncX does not require staining preparation or dissection, with only formalin fixation being necessary. For optical microscopy, the filter membrane or emboli are removed from the CPD or cut off, dehydrated, embedded in paraffin, and mounted onto a glass slide. Thin (5  $\mu\text{m}$  thick) sections are stained with hematoxylin–eosin and Heidenhain trichrome (Angelini *et al.*, 2002; Rogers *et al.*, 2004; Hayashi *et al.*, 2009; Piñero *et al.*, 2009). For scanning electron microscopy, the internal surface of the polyurethane membrane is flattened after being cut off from the CPD. The samples are washed in normal saline solution and distilled water, and dehydrated in alcohol, with a final incubation in amyl acetate, silver nitrate or barium sulfate–gelatin–thymol mixture. They can also be processed for the CO<sub>2</sub> critical dry

point and gold sputtering (DeRubertis *et al.*, 2007; Brightwell *et al.*, 2011).

This study was subject to several limitations, some of which were due to the small study population. We did not observe focal neurologic deficits or CPD-related flow arrest in our small population and therefore could not assess the correlation between clinical outcomes and pcSyncX data. Furthermore, we did not exclude the presence of clinically silent microembolization, because diffusion-weighted MRI was not performed after CAS. There are also some challenges to applying the described method to *in vivo* imaging, mostly due to the fixed direction of the beam. In this study the small samples could be rotated in front of the synchrotron radiation, instead of rotating the beam itself. Future technical innovations, such as the development of a bed that can be rotated around the vertical axis in front of the beam (Castelli *et al.*, 2011) or of a technique for rotating the beam, would make it possible to acquire *in vivo* pcSyncX images of a patient lying on a bed. Another disadvantage of the present technique is that it requires an elaborate manual segmentation or labeling process involving the selection of materials other than the membrane structure of the CPD by visual analysis. Finally, analyses of the absorption density and the phase-contrast factor were not included in the reconstruction algorithm used in this study, whereas edge enhancement using phase contrast plays an important role in microtomography.

## 5. Conclusion

pcSyncX makes it possible to visualize the microscale appearance of embolic debris around the pores of a CPD and can be used to measure both the total debris volume and the amount of debris at different positions along the CPD axis. pcSyncX might eventually be useful in improving the design of CPDs and in modifying the procedural steps so as to reduce the probability of complications.

The authors would like to warmly thank the 7B2 beamline staff and support groups at the Pohang Light Source in Korea for help during the experiments. This work was supported by the Basic Science Research Program through the National Research Foundation of Korea (NRF) funded by the Ministry of Education, Science and Technology (grant number NRF-2011-0014573). Otherwise we have no conflicts of interests to declare.

## References

- Angelini, A., Reimers, B., Della Barbera, M., Saccà, S., Pasquetto, G., Cernetti, C., Valente, M., Pascotto, P. & Thiene, G. (2002). *Stroke*, **33**, 456–461.
- Baldi, S., Zander, T., Rabellino, M., González, G. & Maynar, M. (2011). *Am. J. Neuroradiol.* **32**, 759–763.
- Brightwell, R. E., Ryder, T. A., Hamady, M. & Cheshire, N. J. (2011). *Int. J. Surg.* **9**, 177–182.
- Casserly, I. P., Abou-Chebl, A., Fathi, R. B., Lee, D. S., Saw, J., Exaire, J. E., Kapadia, S. R., Bajzer, C. T. & Yadav, J. S. (2005). *J. Am. Collect. Cardiol.* **46**, 1466–1472.
- Castelli, E., Tonutti, M., Arfelli, F., Longo, R., Quaia, E., Rigon, L., Sanabor, D., Zanconati, F., Dreossi, D., Abrami, A., Quai, E.,

- Bregant, P., Casarin, K., Chenda, V., Menk, R. H., Rokvic, T., Vascotto, A., Tromba, G. & Cova, M. A. (2011). *Radiology*, **259**, 684–694.
- Castriota, F., Cremonesi, A., Manetti, R., Liso, A., Oshola, K., Ricci, E. & Balestra, G. (2002). *J. Endovasc. Ther.* **9**, 786–792.
- CAVATAS Investigators (2001). *Lancet*, **357**, 1729–1737.
- Choi, C.-H., Kim, H.-T., Choe, J.-Y., Kim, S.-K., Choi, G.-W., Jheon, S. & Kim, J.-K. (2010). *J. Synchrotron Rad.* **17**, 393–399.
- Coan, P., Bamberg, F., Diemoz, P. C., Bravin, A., Timpert, K., Mützel, E., Raya, J. G., Adam-Neumair, S., Reiser, M. F. & Glaser, C. (2010). *Invest. Radiol.* **45**, 437–444.
- Cremonesi, A., Manetti, R., Setacci, F., Setacci, C. & Castriota, F. (2003). *Stroke*, **34**, 1936–1941.
- DeRubertis, B. G., Chaer, R. A., Gordon, R., Bell, H., Hyneczek, R. L., Pieracci, F. M., Karwowski, J., Kent, K. C. & Faries, P. L. (2007). *J. Vasc. Surg.* **45**, 716–724.
- EVA-3S Investigators (2004). *Stroke*, **35**, e18–e20.
- Hayashi, K., Kitagawa, N., Morikawa, M., Hiu, T., Morofuji, Y., Suyama, K. & Nagata, I. (2009). *Surg. Neurol.* **72**, 532–537.
- Hill, M. D., Morrish, W., Soulez, G., Nevelsteen, A., Maleux, G., Rogers, C., Hauptmann, K. E., Bonafé, A., Beyar, R., Gruberg, L., Schofer, J. and for the MAVERIC International Investigators (2006). *Am. J. Neuroradiol.* **27**, 759–765.
- Kastrup, A., Gröschel, K., Krapf, H., Brehm, B. R., Dichgans, J. & Schulz, J. B. (2003). *Stroke*, **34**, 813–819.
- Koh, S. B., Suh, S. I., Lee, D. H., Kim, A. R., Oh, C. H., Yoon, J. S., Weon, B. M., Seol, S. K., Pyun, A. R., Je, J. H., Hwu, Y. & Margaritondo, G. (2006). *Neuroimage*, **32**, 566–569.
- Lownie, S. P., Pelz, D. M., Lee, D. H., Men, S., Gulka, I. & Kalapos, P. (2005). *Am. J. Neuroradiol.* **26**, 1241–1248.
- Maynar, M., Baldi, S., Rostagno, R., Zander, T., Rabellino, M., Llorens, R., Alvarez, J. & Barajas, F. (2007). *Am. J. Neuroradiol.* **28**, 1378–1383.
- Meuli, R., Hwu, Y., Je, J. H. & Margaritondo, G. (2004). *Eur. Radiol.* **14**, 1550–1560.
- Müller-Hülsbeck, S., Stolzmann, P., Liess, C., Hedderich, J., Paulsen, F., Jahnke, T. & Heller, M. (2005). *Radiology*, **235**, 454–460.
- Piñero, P., González, A., Martínez, E., Mayol, A., Rafel, E., González-Marcos, J. R., Moniche, F., Cayuela, A. & Gil-Peralta, A. (2009). *Am. J. Neuroradiol.* **30**, 473–478.
- Quan, V. H., Huynh, R., Seifert, P. A., Kuchela, A., Chen, W. H., Sütsch, G., Eisenhauer, A. C. & Rogers, C. (2005). *Am. J. Cardiol.* **95**, 1415–1419.
- Roffi, M., Greutmann, M., Schwarz, U., Luscher, T. F., Eberli, F. R. & Amann-Vesti, B. (2008). *J. Endovasc. Ther.* **15**, 103–109.
- Rogers, C., Huynh, R., Seifert, P. A., Chevalier, B., Schofer, J., Edelman, E. R., Toegel, G., Kuchela, A., Woupio, A., Kuntz, R. E. & Macon, N. D. (2004). *Circulation*, **109**, 1735–1740.
- Shinohara, M., Yamashita, T., Tawa, H., Takeda, M., Sasaki, N., Takaya, T., Toh, R., Takeuchi, A., Ohigashi, T., Shinohara, K., Kawashima, S., Yokoyama, M., Hirata, K. & Momose, A. (2008). *Am. J. Physiol. Heart Circ. Physiol.* **294**, H1094–H1100.
- Sorimachi, T., Nishino, K., Morita, K., Sasaki, O., Koike, T., Ito, Y. & Fujii, Y. (2010). *J. Endovasc. Ther.* **17**, 661–670.
- Sorimachi, T., Nishino, K., Morita, K., Takeuchi, S., Ito, Y. & Fujii, Y. (2011). *Am. J. Neuroradiol.* **32**, 288–293.
- Takeda, T., Momose, A., Hirano, K., Haraoka, S., Watanabe, T. & Itai, Y. (2000). *Radiology*, **214**, 298–301.
- Wholey, M. H., Al-Mubarek, N. & Wholey, M. H. (2003). *Catheter. Cardiovasc. Interv.* **60**, 259–266.
- Yadav, J. S., Wholey, M. H., Kuntz, R. E., Fayad, P., Katzen, B. T., Mishkel, G. J., Bajwa, T. K., Whitlow, P., Strickman, N. E., Jaff, M. R., Popma, J. J., Snead, D. B., Cutlip, D. E., Firth, B. G. & Ouriel, K. for the Stenting and Angioplasty with Protection in Patients at High Risk for Endarterectomy Investigators (2004). *N. Engl. J. Med.* **351**, 1493–1501.